Vibrational properties of the Au-($\sqrt{3} \times \sqrt{3}$)/Si(111) surface reconstruction

B. Halbig,* M. Liebhaber, U. Bass, and J. Geurts
Universität Würzburg, Physikalisches Institut, Experimentelle Physik 3, Am Hubland, 97074 Würzburg, Germany

E. Speiser, J. Räthel, S. Chandola, and N. Esser
Leibniz-Institut für Analytische Wissenschaften - ISAS - e.V., Albert-Einstein-Strasse 9, 12489 Berlin, Germany

M. Krenz, S. Neufeld, and W. G. Schmidt
Universität Paderborn, Department Physik, Warburger Strasse 100, 33098 Paderborn, Germany

S. Sanna
Justus-Liebig-Universität Gießen, Institut für Theoretische Physik, Heinrich-Buff-Ring 16, 35392 Gießen, Germany

(Received 26 September 2017; published 10 January 2018)

The vibrational properties of the Au-induced $(\sqrt{3} \times \sqrt{3})R30^\circ$ reconstruction of the Si(111) surface are investigated by polarized surface Raman spectroscopy and density-functional theory. The Raman measurements are performed *in situ* at room temperature as well as 20 K, and they reveal the presence of vibrational eigenmodes in the spectral range from 20 to 450 cm^{-1}. In particular, two peaks of E symmetry at 75 and 183 cm^{-1} dominate the spectra. No substantial difference between room- and low-temperature spectra is observed, suggesting that the system does not undergo a phase transition down to 20 K. First-principles calculations are performed based on the structural models discussed in the literature. The thermodynamically stable conjugate honeycomb-chained-trimer model (CHCT) [Surf. Sci. **275**, L691 (1992)] leads to phonon eigenvalues compatible with the experimental observations in the investigated spectral range. On the basis of the phonon eigenfrequencies, symmetries, and Raman intensities, we assign the measured spectral features to the calculated phonon modes. The good agreement between measured and calculated modes provides a strong argument in favor of the CHCT model.

DOI: 10.1103/PhysRevB.97.035412

I. INTRODUCTION

Ordered (sub)monolayers of metal adatoms on semiconductor surfaces have attracted great scientific interest due to their exotic properties resulting from reduced dimensionality. These systems have been intensely investigated experimentally as well as theoretically to gain information about low-dimensional physics and correlation effects [1–9]. The electronic properties of such surface layers are directly linked to their atomic structure [10–13], which, in turn, also determines the vibration dynamics [14,15]. Therefore, knowledge of the vibration modes is an essential ingredient for a comprehensive understanding of adsorbate systems and their interplay with the substrate.

Among the well-established adatom systems, Au atoms on crystalline Si(111) surfaces represent an extensively studied example. Depending on the deposition parameters, different reconstructions can be prepared, either one- or two-dimensional [16,17]. In the former case, denoted as Au-(5 × 2)/Si(111) reconstruction, the Au atoms are arranged into chains, whereas in the latter case the Au atoms are ordered in an isotropic two-dimensional pattern. Among the two-dimensional patterns, the most common one has a $(\sqrt{3} \times \sqrt{3})$ periodicity. Recently, this system has been proposed as a platform for two-dimensional topological insulators [18]. One- and two-dimensional reconstructions not only strongly differ in their electronic properties, but they are expected to exhibit quite different dynamics of the adatom vibrations. While the lattice vibrations of the Au-(5 × 2)/Si(111) chains have been explored previously [19], no information is available concerning the vibrational properties of the other Au-induced reconstructions. To improve our knowledge of this prime example of low-dimensional physics, we study in this work the lattice dynamics of the two-dimensional reconstruction of one-monolayer Au on a Si(111) substrate, currently referred to as Au-$(\sqrt{3} \times \sqrt{3})R30^\circ$/Si(111), by means of Raman spectroscopy and density-functional theory (DFT).

A detailed consideration of the atomic structure of the Au-$(\sqrt{3} \times \sqrt{3})R30^\circ$/Si(111) system investigated in this paper is necessary to understand its lattice dynamics. Many different structural models possibly describing the experimental observations have been proposed in the past [20]. The most relevant among these models are depicted in Fig. 1 and described briefly in the following. The twisted-trimer (TT) model by Chester *et al.* [21,22], shown in Fig. 1(a), was developed through medium-energy ion scattering and Monte Carlo simulations. The conjugate honeycomb-chained-trimer (CHCT) model by Ding *et al.* [23], depicted in Fig. 1(b), results from DFT calculations within the local-density approximation. The honeycomb-chained-trimer (HCT) model by Zhang *et al.* [24], displayed in Fig. 1(c), was proposed after angle-resolved photoelectron measurements. Finally, the

*benedikt.halbig@physik.uni-wuerzburg.de

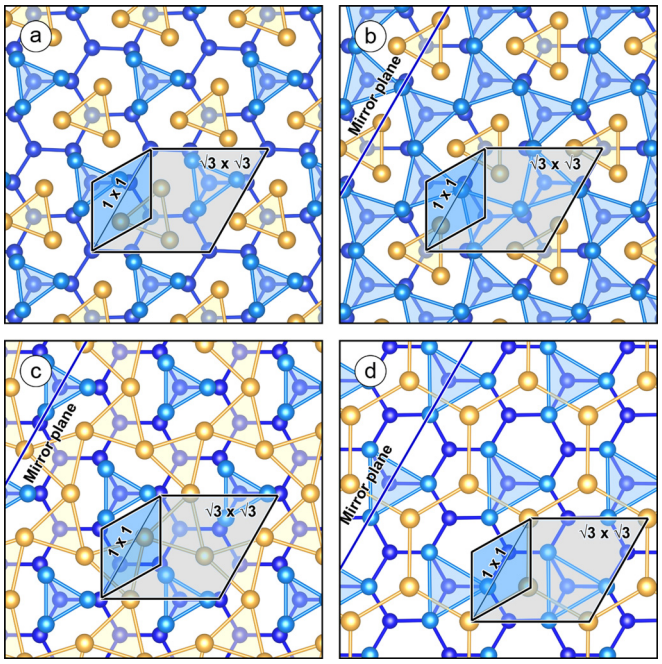

FIG. 1. Structural models of the Au-$(\sqrt{3} \times \sqrt{3})R30^\circ$ reconstruction on Si(111). (a) Twisted-trimer (TT) model, (b) conjugate honeycomb-chained-trimer (CHCT) model, (c) honeycomb-chained-trimer (HCT) model, and (d) H_3-missing-top-layer (H_3-MTL) model. Au atoms in yellow, Si atoms in blue, and topmost Si atoms in light blue. The substrate (1×1) and the $(\sqrt{3} \times \sqrt{3})$ reconstructed surface unit cells as well as mirror symmetry planes are indicated. See text for further details.

H_3-missing-top-layer (H_3-MTL) model by Kadohira *et al.* [25], shown in Fig. 1(d), is a result of first-principles calculations within the local-density approximation. The first three models (TT, CHCT, and HCT) feature three Au atoms per surface unit cell and thus model a coverage of 1.0 Au monolayer (ML). All these models are characterized by a trimer of Au atoms close to the H_3 positions. The topmost Si layer also builds trimers. The three models differ in size and orientation of the Au and Si trimers against each other. The relative trimer orientation furthermore determines the surface symmetry. The CHCT and HCT models possess a mirror symmetry plane [shown in Figs. 1(b) and 1(c)], which is missing in the TT model. The fourth structure (H_3-MTL) models a lower Au coverage of 0.66 ML. It displays a hexagonal structure of Au atoms on the surface. In the middle of the hexagon, the Au atom corresponding to the H_3 position is missing, resulting in two Au atoms per surface unit cell. Similarly to the CHCT and HCT structures, the H_3-MTL model possesses a mirror symmetry plane, as shown in Fig. 1(d). In all the proposed models, the Au atoms form a flat layer atop the Si surface and show no corrugation. Structural patterns corresponding to a larger (6×6) surface reconstruction formed at an Au coverage exceeding 1 ML are also reported [26,27], however they are not a subject of the present investigation.

Basically, spectroscopic measurements of the vibration dynamics of clean surfaces and adsorbate layers are a challenging task. This is due to the fact that the scattering region only consists of a small volume. The most established experimental tools for analyzing surface and adsorbate vibrations are intrinsically surface-sensitive techniques, such as high-resolution electron-energy-loss spectroscopy (HREELS) [28–30] and helium atom scattering (HAS) [31,32]. Results from these methods have been published for, e.g., the clean (7×7)-reconstructed Si(111) surface [33,34]. Optical methods such as transmission infrared spectroscopy (TIRS) have also been applied successfully to surface systems [35,36].

Raman spectroscopy, as an optical method, is not intrinsically surface-specific, but its sensitivity has been proven to be sufficient for the investigation of extremely thin surface films [37] and adatom systems [38–42]. In the following, this application of Raman spectroscopy will be denoted as surface Raman spectroscopy (SRS). SRS can give information on vibration modes that is complementary to HREELS and HAS, e.g., high spectral resolution and symmetry properties of the vibration eigenmodes. Recently, the Au-(5×2)/Si(111) reconstruction has been studied by SRS in combination with first-principles calculations [19]. SRS studies of clean surfaces haven been published for the (7×7)-reconstructed Si(111) surface [43] and various further clean and adsorbed surfaces [44–46].

Surface Raman spectroscopy becomes a particularly powerful tool for surface investigation when supported by atomistic calculations. Indeed, Raman frequencies as well as selection rules are strongly related to the surface structure, and they represent reliable criteria to validate or rule out competing structural models. The comparison of the measured frequencies with surface phonon calculations for candidate geometries may thus lead to structural identification and, more generally, to the assignment of calculated eigenvectors of the individual vibration modes to the measured Raman peaks. Unfortunately, an assignment based on frequency and symmetry configurations is often difficult, since the surface systems are typically of low symmetry, and the calculations yield a large number of phonons with different degrees of surface localization. To achieve a reliable assignment, we have previously implemented algorithms for the calculation of the Raman scattering efficiency, which have proven to be useful for the interpretation of Raman spectra of bulk materials [47] as well as low-dimensional Au structures at the Si(111) surface [19].

In this work, we report on the observation and identification of the surface vibration eigenmodes of the monolayer Au-$(\sqrt{3} \times \sqrt{3})R30^\circ$ reconstruction on the Si(111) surface, most of them in the range 20–200 cm^{-1}, containing all Au-related vibration modes. The lattice dynamics is investigated by polarized *in situ* Raman spectroscopy under ultrahigh-vacuum (UHV) conditions and first-principles calculations yielding vibration eigenfrequencies and eigenvectors as well as their Raman intensities. After an explanation of the experimental details and calculation techniques, we discuss the appearance of characteristic modes of the Au covered Si(111) surface in contrast to the aged Si(111) surface. Polarized spectra at room temperature and low temperature are compared to DFT calculations for the TT and CHCT model, which we find to be thermodynamically stable. The CHCT model leads to phonon frequency eigenvalues compatible with the measurements, while the TT model shows large deviations from the experimental values. Calculated and measured spectra for the CHCT

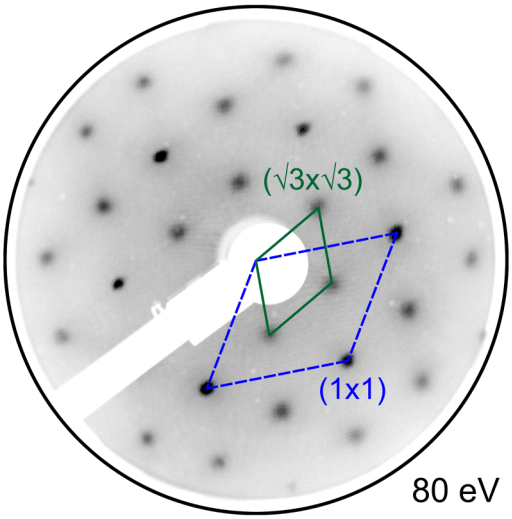

FIG. 2. LEED pattern of Au-($\sqrt{3} \times \sqrt{3}$)$R30°$/Si(111) at room temperature. Electron energy $E = 80$ eV. The blue and green rhomb denote the (1 × 1)- and the Au-($\sqrt{3} \times \sqrt{3}$)$R30°$ unit cell, respectively.

structure are found to be in good agreement, which yields an argument for this model and allows for the identification and assignment of the measured spectral features.

II. EXPERIMENT AND CALCULATION METHODOLOGY

Polished highly doped Si(111) was used as a sample substrate. After an *ex situ* wet-chemical cleaning procedure [43], the samples were degassed *in situ* for several hours. For the preparation of the clean (7 × 7) surface reconstruction, the samples were heated by direct current in a flash annealing process up to $T = 1550$ K. The temperature was checked by a pyrometer (emissivity 67%). In a second step, Au was deposited onto the Si(111) surface by an e-beam evaporator up to a coverage $\geqslant$1.0 ML, measured with a quartz crystal microbalance. During deposition, the sample was held at an elevated temperature ($T \approx 800$ K). The Au-($\sqrt{3} \times \sqrt{3}$)$R30°$/Si(111) reconstruction was obtained by subsequent annealing. The applied annealing temperature was ≈900 K and ensured the desorption of excess adatoms to get a final coverage of ≈1.0 ML. After preparation, the quality of the reconstruction was checked by low-energy electron diffraction (LEED). The resulting LEED pattern (Fig. 2) shows a clear ($\sqrt{3} \times \sqrt{3}$) reconstruction without any sign of a (5 × 2) admixture. In line with the Au/Si(111) phase diagram of Ref. [48], the total absence of a (5 × 2) signature indicates Au coverage at least well above 0.76 ML.

The Raman spectra of Au-($\sqrt{3} \times \sqrt{3}$)$R30°$/Si(111) were obtained *in situ* under UHV conditions immediately after preparation (base pressure $p < 1 \times 10^{-10}$ mbar). For these spectra, two separate Raman setups with different facilities were employed. The setup for spectra at room temperature (RT) consisted of a solid-state laser that used the 660 nm line (≅1.87 eV) with a power of 300 mW. The scattered light was collected by a modified DILOR-XY triple spectrometer, which enabled the registration of Raman intensity down to 13 cm^{-1} from the laser line. The other setup, which was essentially applied for measurements at low temperature (LT), i.e., $T \approx 20$ K, employed an Ar^+ ion laser that was operated with the 488 nm line (≅2.54 eV) with 120 mW laser power. Here, the Raman light was analyzed by a SPEX 1000M single monochromator after passing an ultrasteep longpass edge filter (SEMROCK RazorEdge), which allowed spectra down to 45 cm^{-1} toward the laser line. Low temperatures were obtained by cooling with a continuous-flow He cryostat. Both setups were equipped with high-efficiency Si-based CCD detectors (ANDOR iDus series) and were operated in near-backscattering geometry. The spectral resolution was 3 cm^{-1}.

To analyze the symmetry properties of the vibration modes, Raman spectra were recorded with well-defined linear polarization of the incident and scattered light. They are labeled according to the Porto notation [49,50]: backscattering from a z-oriented surface with incoming and scattered polarization directions e_i and e_s, respectively, is denoted as $z(e_i e_s)\bar{z}$. The laser beam was polarized vertically, indicated as x, while the scattered light was analyzed either in x or y polarization. If no polarization analyzer was employed, both configurations were measured simultaneously [notation for unpolarized spectra: $z(xx)\bar{z} + z(xy)\bar{z}$].

A detailed analysis of the measured peak properties includes polarization dependences and group-theoretical considerations. The threefold two-dimensional surface space group of Au-($\sqrt{3} \times \sqrt{3}$)$R30°$/Si(111) is $p31m$ (corresponding to the three-dimensional point group C_{3v}) [51] for the CHCT-, HCT-, and H3-MTL model, and $p3$ (corresponding to C_3) for the TT model. Since with regard to Raman spectroscopy the point groups C_3 and C_{3v} behave alike, we consider in the following only the latter. According to the character table of the group C_{3v}, there are two nondegenerate modes, A_1 and A_2, and a doubly degenerate mode E [52]. Modes with A_2 symmetry are silent modes, i.e., optically inactive. The modes of A_1 and E symmetry are Raman-active instead. According to the basis functions of the irreducible representations (finding its counterpart in the Raman tensor [53]), the A_1 modes (basis functions $x^2 + y^2, z^2$) are only visible in a $z(xx)\bar{z}$ configuration, while the E mode [basis functions $(x^2 - y^2, xy)$ and (yz, xz)] are visible in both polarization configurations, $z(xx)\bar{z}$ and $z(xy)\bar{z}$ [50]. The latter basis function of E has no relevance in our experiments in backscattering geometry on the z-oriented surface since it contains a z-direction contribution.

The Au structures on the Si(111) surface are modeled within the DFT, as implemented in the Vienna ab initio simulation package (VASP) [54,55]. Thereby, we perform total-energy calculations both within the local-density approximation (LDA) [56,57] and within the generalized gradient approximation (GGA) in the Perdew-Burke-Ernzerhof (PBE) formulation [58,59] in order to estimate the influence of the calculation details on our results. Projector augmented wave (PAW) potentials [60,61] with projectors up to $l = 1$ for H, $l = 2$ for Si, and $l = 3$ for Au are used. The number of valence electrons that were employed for the simulation of the H, Si, and Au atoms amounted to 1 ($1s^1$), 4 ($3s^2 3p^2$), and 11 ($5d^{10} 6s^1$), respectively. The electronic wave functions are expanded into plane waves up to an energy cutoff of 500 eV. A 12 × 12 × 1 Monkhorst-Pack [62] k-point mesh was used to perform the integration in the Brillouin zone (BZ).

The Si surfaces are modeled with asymmetric slabs consisting of six Si bilayers stacked along the [111] crystallographic direction modeling the substrate, the surface termination including the Au layer, and a vacuum region of about 20 Å. H atoms saturate the dangling bonds at the backside face of the slabs. The atomic positions are relaxed until the residual Hellmann-Feynman forces are below 0.01 eV/Å. Three Si bilayers and the H atoms are kept constrained in order to model the substrate, while the Au layer and the remaining Si atoms are allowed to relax.

The lattice dynamics is calculated in two stages. In a first step, the vibrational displacement patterns as well as the eigenfrequencies of the zone-center optical phonons are calculated within the frozen phonon method [63]. The convergence of the phonon eigenvalues with respect to the number of mobile atomic layers is thereby tested. The calculated phonon eigenfrequencies depend to some extent on the details of the calculations, such as the exchange-correlation functional or the substrate lattice constant. We have calculated the phonon modes both with the LDA and the GGA, employing the respective calculated equilibrium lattice constant as well as the experimental lattice constant. We show in this work the values calculated at the experimental Si lattice constant. The frequencies calculated with the different approaches agree for most phonons within a few cm^{-1}. The largest calculated deviation between DFT-LDA and DFT-GGA amounts to 9 cm^{-1}, which is considered the uncertainty of the method. In a second step, the differential Raman-scattering efficiency is calculated following the formalism that was employed also in Refs. [19,47] and is described in detail in Refs. [50,64]. The central quantity in this approach is the Raman susceptibility tensor α^m,

$$\alpha_{ij}^{m} \propto \sum_{\kappa,\beta} \frac{\partial \chi_{ij}^{(1)}}{\partial \tau_{\kappa\beta}} u_m(\kappa\beta), \tag{1}$$

where $u_m(\kappa\beta)$ are the eigenvectors and $\tau_{\kappa\beta}$ represents the displacement of atom κ in direction β within the phonon mode m. $\chi_{ij}^{(1)}$ is the electronic linear dielectric susceptibility tensor, which is related to the frequency-dependent dielectric permittivity, in CGS units, by $\varepsilon_{ij}^{(1)} = 1 + 4\pi\chi_{ij}^{(1)}$. The imaginary part of the frequency-dependent dielectric tensor is calculated within the independent-particle approximation [65] by a summation over empty states. This requires an accurate checking of the convergence of the dielectric function with respect to the total number of bands. We employ 2000 bands in our models, which yields a convergence up to 10^{-3}. Due to computational limitations, quasiparticle and excitonic effects are not included in our computation of the dielectric tensor. This will affect the calculated spectra by introducing some error that is hard to quantify.

III. RESULTS AND DISCUSSION

A. Surface structure

After the preparation procedure, the LEED pattern for each Au/Si(111) sample was registered for a quality check of the reconstruction. Therefore, a mixture of one-dimensional (5 × 2)-Au chains and two-dimensional ($\sqrt{3} \times \sqrt{3}$)-Au-induced reconstructions can be ruled out. The LEED pattern for Au-($\sqrt{3} \times \sqrt{3}$)$R30^\circ$ obtained at RT with an electron energy of 80 eV is shown in Fig. 2. The very sharp superstructure spots of the ($\sqrt{3} \times \sqrt{3}$) reconstruction are marked by the green rhomb, which is rotated by 30° with respect to the blue rhomb of the (1 × 1) unit cell. The edge lengths of the rhombs differ by a factor $\sqrt{3}$, confirming the notation as ($\sqrt{3} \times \sqrt{3}$)$R30^\circ$. The Au trimers that constitute this reconstruction are shown in the real-space picture in Fig. 1.

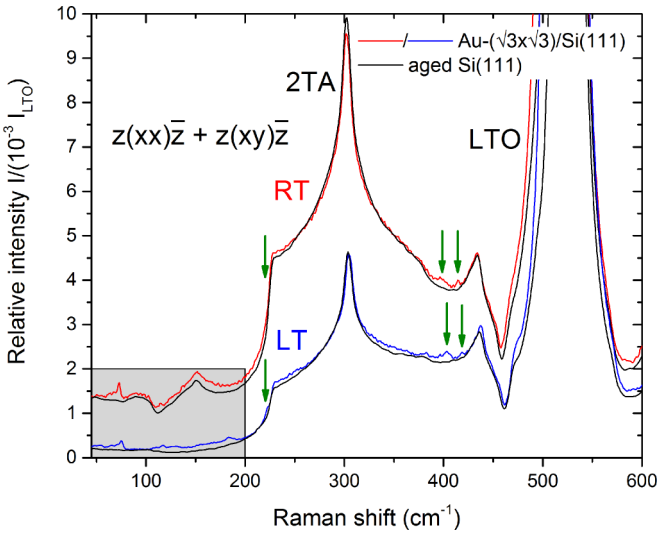

FIG. 3. Waterfall plot of the Raman spectra of Au-($\sqrt{3} \times \sqrt{3}$)$R30^\circ$/Si(111) for the polarization configuration $z(xx)\bar{z} + z(xy)\bar{z}$ for room temperature (RT, red) and $T \approx 20$ K (LT, blue). For both cases, as a reference the aged and unreconstructed Si(111) is plotted (black). The additional intensity features of the Au-covered surfaces are attributed to the Au-($\sqrt{3} \times \sqrt{3}$) reconstruction. The highlighted spectral range up to 200 cm^{-1} is analyzed in more detail and plotted on an extended frequency scale in the following figures. The green arrows indicate Au-induced features at higher frequencies.

B. Surface Raman spectra

In Fig. 3, nonpolarized Raman spectra over a wide spectral range are plotted for RT and LT. Together with the spectra of the Au-reconstructed surface, those of the aged and hence unreconstructed Si(111) surface are shown as a reference. This aging procedure consists of an exposure to higher pressure ($p \geqslant 10^{-8}$ mbar) for several minutes, and it was explained in more detail in Ref. [19]. After aging, no structured LEED pattern of a reconstructed surface was found. For all surfaces, the most prominent features are identified as bulk vibration modes from the Si substrate [66,67]. The most dominant bulk Si mode by far is the degenerate longitudinal and transverse optical phonon (LTO), located at 520 cm^{-1}. Its peak intensity exceeds the vertical scale of the figure by a factor of about 10^2. The second-order process of the transversal acoustical phonons (2TA) is centered around 300 cm^{-1}. Its intensity maximum is attributed to the X point in the BZ, the kinks left and right originate from the L and W point, respectively. Below 200 cm^{-1}, we observe the most striking differences between the Au-reconstructed and -unreconstructed surface. Because of the high atomic mass of Au (mass number $A = 197$), it

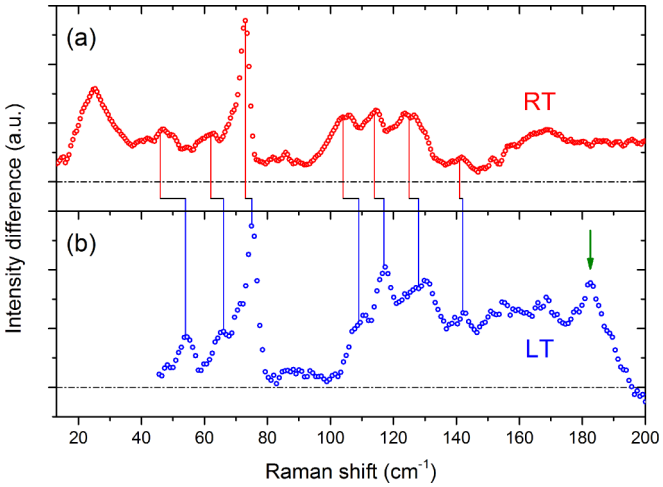

FIG. 4. Raman intensity difference between the Au-($\sqrt{3} \times \sqrt{3}$)$R30°$/Si(111) and the unreconstructed Si(111) reference surface for the polarization configuration $z(xx)\bar{z} + z(xy)\bar{z}$: (a) room temperature (RT), (b) low temperature (LT, $T \approx 20$ K). The phonon peaks shift slightly to higher wave numbers after cooling. Note the arising peak at 183 cm^{-1} (green arrow) at LT.

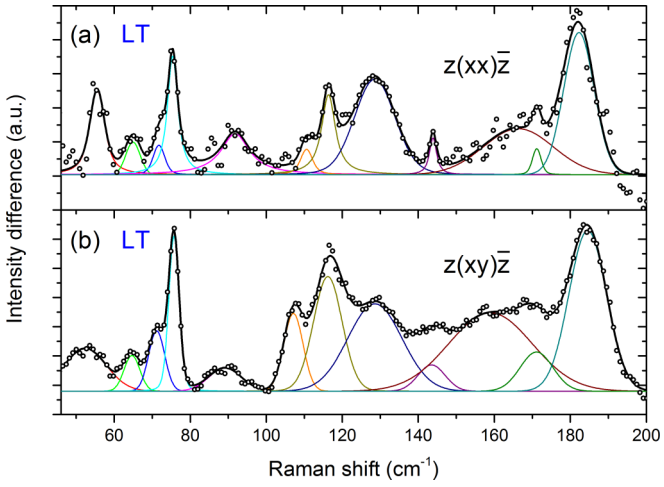

FIG. 5. Polarization-dependent difference spectra of Au-($\sqrt{3} \times \sqrt{3}$)/Si(111) for low temperature (LT, $T \approx 20$ K): (a) polarization configuration $z(xx)\bar{z}$, (b) polarization configuration $z(xy)\bar{z}$. The spectra are fitted with Voigt profiles (full lines) and plotted together with the cumulative fit (black).

is this low-frequency range where those vibration modes are expected that are dominated by Au atom oscillations, while vibrations of the rather light Si atoms (mass number $A = 28$) should occur predominantly at higher frequencies. Therefore, the following analysis will focus on the frequency range from about 20 to about 200 cm^{-1} (see, e.g., Fig. 4). Further features are observed at 217, 221, 397, and 414 cm^{-1}. These peaks are labeled with green arrows in Fig. 3. Their frequencies for RT and LT are listed in Table II.

The net contribution of the Au-($\sqrt{3} \times \sqrt{3}$)$R30°$ reconstruction, i.e., the Raman intensity difference between the Au-reconstructed surface and the unreconstructed Si(111) reference surface, is plotted in Fig. 4 in the unpolarized configuration, i.e., $z(xx)\bar{z} + z(xy)\bar{z}$. The main peak of the RT spectrum [Fig. 4(a)] is located at 73 cm^{-1} and has a shoulder on the low-frequency side. Another dominant feature is the group of three peaks located at 104, 114, and 125 cm^{-1}. Furthermore, there are additional peaks at 46 and 62 cm^{-1}, and a broad feature at about 170 cm^{-1}. All peaks are listed in Table II. The spectrum at LT [Fig. 4(b)] shows only slight differences from the RT spectrum, apart from the temperature-induced peak energy differences due to anharmonic effects. The most striking difference is the peak at 183 cm^{-1}, which arises in the LT spectrum. Generally, the spectral shape above 150 cm^{-1} is more structured at LT with respect to the rather flat behavior at RT. This aspect will be discussed in more detail in the context of the peak fits below. Moreover, it should be noted that no significant changes in the Raman spectra, which would indicate structural transitions, are observed down to $T \approx 20$ K.

To determine the symmetry properties of the vibration modes, we have plotted the polarized LT spectra for $z(xx)\bar{z}$ and $z(xy)\bar{z}$ separately in Figs. 5(a) and 5(b). The spectra were fitted with Voigt profiles in order to evaluate the individual contributions of the peaks in more detail. The cumulative fit (black curve) in each spectrum shows the sum over the Voigt profiles. Although each peak of one polarization configuration finds its counterpart in the other one, the relative intensities of the peaks within each spectrum are specifically determined by the polarization configuration. Hence we will denote peaks with predominant intensity in a $z(xx)\bar{z}$ configuration as A_1 modes. Accordingly, peaks with approximately the same intensity in both panels will be labeled as E modes. The most obvious polarization-induced variation occurs for the intensity ratio of the peak at 128 cm^{-1} to its left-side neighbor peak. In the $z(xx)\bar{z}$ configuration this ratio is much higher, and already in the direct view of the spectrum the 128 cm^{-1} peak appears much more pronounced. Therefore, it is identified as an A_1 mode. All other peaks show no clear polarization dependence and are considered as E-like. These symmetry labels are listed in Table II. The full width at half-maximum (FWHM) of the fit contribution at about 165 cm^{-1} is unusually high, which may be due to a superposition of spectrally closely spaced structures. This phenomenon is even more pronounced at RT [Fig. 4(a)] where the spectral shape above about 155 cm^{-1} appears as a broad continuum. Due to the high signal intensity, both in $z(xx)\bar{z}$ and $z(xy)\bar{z}$ polarization, we tentatively assign a peak to the feature at 169 cm^{-1}, which is later confirmed by theory. However, due to the large noise in this region, here caution must be taken in the interpretation. The prominent peak at about 183 cm^{-1} appears slightly shifted if both polarization configurations are compared. This may result from the fact that this peak is located spectrally at the steep onset of the second-order 2TA structure of the Si substrate (see Fig. 3). The latter occurs strongly for $z(xx)\bar{z}$ polarization, but much weaker for $z(xy)\bar{z}$ (see also Ref. [43]). Therefore, the subtraction of the stronger steep bulk background in the $z(xx)\bar{z}$ case may shift slightly the peak position in the difference spectrum in Fig. 5(a).

C. Results of first-principles calculations

To identify the thermodynamically stable structure modeling the Au-($\sqrt{3} \times \sqrt{3}$)/Si(111) reconstruction, we have calcu-

TABLE I. Formation energy of the investigated monolayer coverage structures for different XC potentials, given in eV per surface unit cell and with respect to the CHCT model. $LDA^{(eq)}$ and $GGA^{(eq)}$ label LDA and GGA calculations with the corresponding calculated equilibrium lattice constant, while $LDA^{(exp)}$ and $GGA^{(exp)}$ indicate the calculations performed with the experimentally measured lattice constant. The HCT structure is not stable and relaxes either to the TT or to the CHCT geometry.

Structure	$LDA^{(eq)}$	$GGA^{(eq)}$	$LDA^{(exp)}$	$GGA^{(exp)}$
TT		0.085		0.022
CHCT	≡0	≡0	≡0	≡0
HCT				

lated the formation energy for the different models discussed in the literature. As the structural and energetic differences among the discussed models are rather small, the calculations have been performed both within DFT-GGA and DFT-LDA employing the corresponding equilibrium lattice constant as well as within the LDA and the GGA with the experimentally measured Si lattice constant. In this way, we have checked the effect of the computational parameters on our results. The outcome of our calculations concerning the stability of the ML Au structures is shown in Table I. Irrespective of the XC functional, the CHCT model shows the lowest formation energy. In agreement with Lee and Kang [20], the HCT structure is found to represent a saddlepoint of the energy landscape and relaxes either to the TT or to the CHCT model. The TT model is only stable within DFT-GGA and is less favorable than the CHCT model by roughly 85 meV per unit cell, or 22 meV per unit cell if the substrate lattice constant is constrained to the experimental value. The calculated energy difference between the CHCT and the TT model is of the same magnitude as in previous calculations [20,25,27].

The stability of the submonolayer H_3-MTL phase has been investigated as well. We find this phase to be a stable structure on the potential energy surface, both within the LDA and the GGA. According to our calculations, it is energetically favored for Au-poor preparation conditions, while Au-rich conditions stabilize the CHCT. This is in excellent agreement with similar calculations by Kadohira *et al.* [25]. Yet, as our measurements are performed for Au monolayer structures, we only show in this work the vibrational spectra calculated for the 1 ML models.

The frozen phonon calculations yield a large number of phonon modes. They can be divided into *A* modes, which are nondegenerate and preserve the threefold rotational symmetry, and *E* modes, which are twofold degenerate and reduce the crystal symmetry. We consider as surface localized modes those phonons whose eigenvectors are localized by 75% or more within the topmost three atomic layers. The number of calculated surface localized modes still exceeds the number of measured spectral features, as not all surface localized modes are Raman-active (e.g., A_2 modes) and some modes have vanishing scattering efficiency within the employed scattering geometry and laser wavelength. To assign the measured peaks to the calculated phonon modes, we calculate the individual scattering efficiencies for the latter at the given excitation frequency and construct a theoretically calculated surface Raman spectrum. However, special care must be given to the proper choice of the excitation wavelength.

The measured Raman spectra depend strongly on the photon energy of the exciting laser. In particular, each phonon mode is coupled to certain electronic states that may or may not be involved in the excitation process, depending on their energy. The Raman efficiency of each mode has thus a particular dependence on the laser wavelength, which is neither linear nor monotonic. As the dielectric tensor employed in the estimation of the Raman intensities is calculated as a sum over electronic states, the DFT models are in principle able to reproduce the Raman peak intensity dependence on the laser wavelength. Unfortunately, the DFT typically underestimates the band gap of Si by about 0.5 eV [68], resulting in a corresponding redshift of the calculated dielectric function with respect to the experiment. A pragmatic way to take into account this artifact is to rigidly shift the eigenvalues by 0.5 eV, as was previously done, e.g., for the calculation of RAS [69] or Raman [19] spectra of Au chains on the Si(111) surface. In practice, we calculate the Raman spectra for an incident photon energy of about 2 eV, which, after the above-explained correction, matches the photon energy of 2.54 eV, corresponding to the wavelength of 488 nm employed in the LT experiment.

The spectra are calculated according to the following procedure. At first, we assign the measured spectral features to the calculated phonon modes on the basis of their frequencies, Raman intensities, and symmetries. Then the spectra are calculated as a sum of Voigt profiles centered at the calculated frequencies and with the calculated height. Thereby we assign a FWHM corresponding to the measured value. The results of this procedure are shown in Fig. 6 for the spectra calculated according to the CHCT model and the TT model in an (xx) polarization configuration in the range between 40 and 210 cm^{-1}. The spectra are directly comparable with the measurements shown in Fig. 5(a). The spectrum calculated for the TT model shows large deviations from the experiment. On the contrary, considering the approximations in our theoretical approach and the difficulty of the experiments, the spectrum calculated for the CHCT model is in satisfactory agreement with the corresponding measured data and allows for their interpretation.

D. Discussion

The frozen-phonon calculations for the CHCT and TT structural models show roughly corresponding eigenvectors, as the structural elements such as Au and Si trimers are common to the two models. Representative modes for the CHCT model are shown in Fig. 7. The main differences between the two models are observed in the phonon eigenfrequency values, as the relative orientation of the Au and Si trimers results in bonds of different strength at the two surfaces. An illustrative example is given by the phonon shown in Fig. 7(c), consisting in a symmetric expansion (breathing mode) of the Au trimer. Within the CHCT model, the Au movement is limited by the presence of Si atoms that are located exactly in the direction of the displacement. Within the TT model instead, this expansion is not constrained by the presence of other atoms, as due to the rotation of the Si trimers the Si atoms are no longer in the

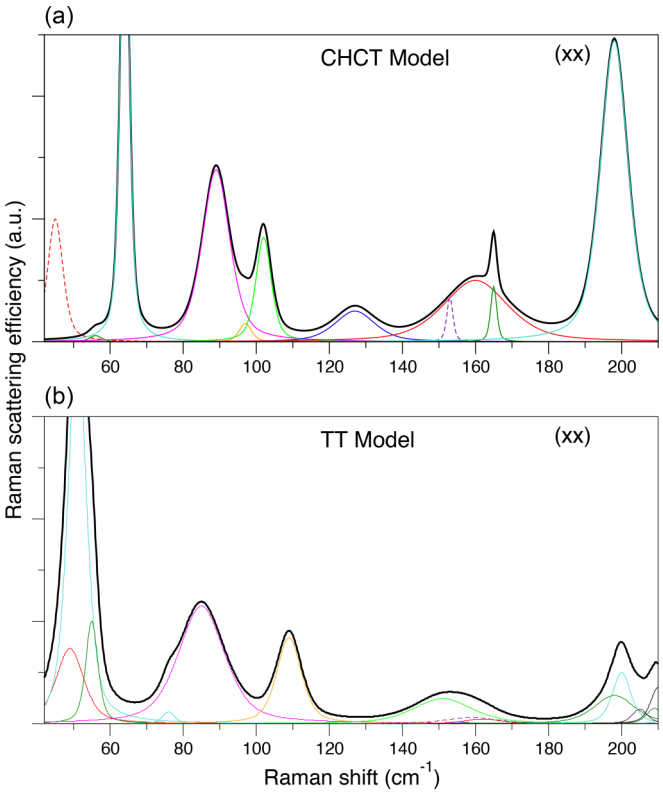

FIG. 6. Raman spectrum of the Au-($\sqrt{3} \times \sqrt{3}$)/Si(111) surface reconstruction calculated for the (xx) polarization according to the (a) CHCT model and the (b) TT model within the DFT-GGA. Dashed lines show experimentally observed features that have vanishing intensity in our calculations. They do not contribute to the cumulative spectrum (black).

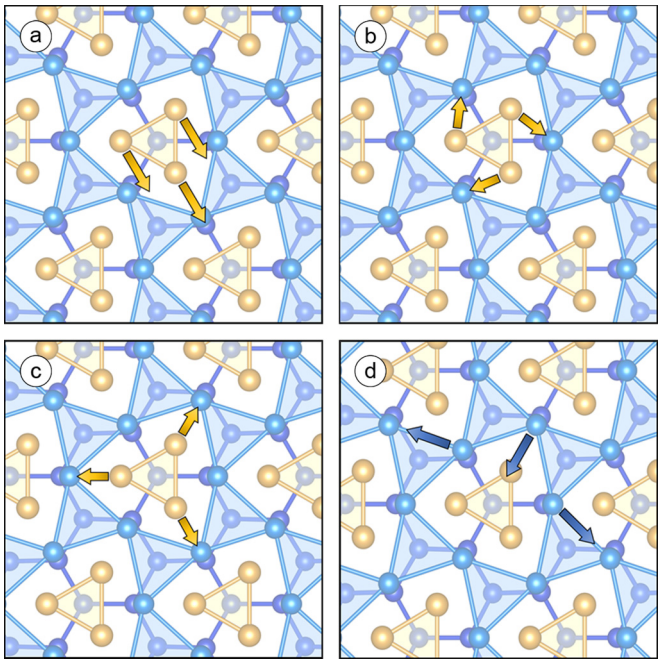

FIG. 7. Displacement pattern of selected phonon modes in the CHCT structure calculated within DFT-GGA at (a) 17, (b) 45, (c) 128, and (d) 205 cm^{-1}. The arrows show the atomic displacement within the ($\sqrt{3} \times \sqrt{3}$) surface unit cell. The symmetry-preserving modes [(b) and (c)] are A-type, the symmetry-reducing ones [(a) and (d)] are E-type.

direction of the displacement [see Fig. 1(a)]. Thus, while this mode has a calculated frequency of about 85 cm^{-1} in the TT structure, it is much harder within the CHCT model, with a frequency of 127 cm^{-1} (see Table II).

Despite roughly comparable phonon eigenvectors, the TT model shows phonon eigenvalues that are not in agreement with the measured values. While the low-frequency, Au-related vibrations roughly match the measured values, the absence of surface localized phonons with frequencies in the range between 109 and 151 cm^{-1}, as well as between 209 and 242 cm^{-1}, is hardly compatible with the experimental data shown in Fig. 5, where different peaks appear in this range. Moreover, different vibrations in the range between 200 and 209 cm^{-1} are predicted for the TT model, but they are not observed in the experiment. The calculated relative intensity of the Raman peaks [shown in Fig. 6(b)] does not reproduce the measured spectrum shown in Fig. 5(a). In particular, the absence of spectral features of outstanding intensity between 190 and 200 cm^{-1} is in striking contrast with the measurements. The CHCT model, instead, allows us to assign each calculated frequency to a measured phonon and vice versa, as shown in Table II and Fig. 6.

Given the approximative character of the models and the challenge of the experiments, the calculated spectrum for the CHCT model in (xx) polarization [shown in Fig. 6(a)] agrees well with the corresponding measured data shown in Fig. 5(a). Two peaks of outstanding intensity with E and A_1 symmetry can be identified at 64 and 198 cm^{-1}, respectively, corresponding to the measured peaks at 75 and 183 cm^{-1}. The first peak is due to a displacement pattern of the Au atoms along the z direction causing a buckling of the Au layer, while the second is a vertical breathing elongation of the Si layer accompanied by minor lateral and symmetric breathing of the Au trimers. A difference between theory and experiment is the occurrence of a shoulder for the peak of E symmetry at 75 cm^{-1} in the measured spectra, which has no counterpart in theory. As no mode (neither a surface-localized mode nor bulk resonance) of similar frequency results from our calculations, this shoulder might originate from the splitting of the main E mode at 75 cm^{-1}. This might be caused, in turn, by structural aspects (adsorbates, domain boundaries, etc.) lifting the degeneracy of the mode.

Between these two main peaks, all peaks with nonvanishing Raman intensity can be identified, appearing in the measured spectra at 90, 109, 117, 128, 142, 155, and 169 cm^{-1}. They correspond to a substrate shear mode (90 cm^{-1}), a breathing mode of the Au trimers without and with substrate involvement (109 and 128 cm^{-1} [Fig. 7(c)]), a distortion of the Au trimers without and with substrate involvement (117 and 169 cm^{-1}), a torsion of the Au trimers accompanied by a vertical movement of the underlying Si layer (142 cm^{-1}), and a vertical displacement of the Si layer (155 cm^{-1}). Experimentally, the fit of the spectra in the spectral range around 165 cm^{-1} by a single mode requires an unusually large FWHM of about 20 cm^{-1} (see Fig. 5). Moreover, such a single mode would experience a blueshift from LT to RT, which is even more peculiar. Therefore,

TABLE II. Experimental and theoretical peak frequencies (in cm^{-1}) of Au-($\sqrt{3} \times \sqrt{3}$)$R30°$/Si(111). Displayed are the experimental room-temperature (RT) and low-temperature (LT) peak positions together with the peak symmetry as described in the text. Theoretical values are shown for the energetically stable models CHCT and TT within the DFT-GGA. "Int." labels the calculated Raman scattering efficiency, normalized to the highest peak of each spectrum. "Loc." denotes the localization of a mode at the Au layer (Au), the Si layer (Si), or in between (Mix.). Calculated modes with vanishing Raman intensity or no surface localization are omitted.

Experiment			Theory							
			CHCT				TT			
RT	LT	Sym.	Freq.	Int.	Sym.	Loc.	Freq.	Int.	Sym.	Loc.
			17	0.759	*E*	Au	16	0.093	*E*	Au
25		?	33	0.001	*A*	Au	33	0.387	*A*	Au
46	54	*E*	45	0.253	*A*	Au	49	0.196	*E*	Mix.
62	66	*E*	55	0.013	*E*	Mix.	51	1.000	*A*	Au
69	71	*E*	64	1.000	*E*	Mix.	55	0.267	*E*	Au
73	75	*E*					76	0.031	*E*	Au
85	90	*E*	89	0.354	*E*	Si	85	0.307	*A*	Au
104	109	*E*	97	0.038	*A*	Mix.	109	0.224	*A*	Au
114	117	*E*	102	0.215	*E*	Au				
125	128	A_1	127	0.063	*A*	Au	151	0.065	*E*	Si
141	142	*E*	153	0.013	*A*	Mix.	157	0.002	*A*	Mix.
170	155	*E*	160	0.127	*A*	Si	159	0.016	*A*	Si
	169	*E*	165	0.114	*E*	Mix.	162	0.012	*A*	Mix.
	183	*E*	198	0.620	*A*	Mix.	198	0.073	*A*	Mix.
							200	0.133	*E*	Mix.
							205	0.037	*E*	Si
							209	0.040	*E*	Mix.
							209	0.095	*A*	Mix.
217	219	A_1	205		*E*	Si				
221	222	*E*	221		*E*	Mix.	242		*A*	
397	401	A_1	400		*A*	Si				
414	419	A_1	417		*A*	Si	413		*A*	

it is supposed that we are dealing with a superposition of distinct closely spaced modes that moreover show a different temperature dependence. This interpretation is corroborated by the calculations, which predict modes of similar frequencies at 161 cm^{-1} with vanishing Raman scattering efficiency, which, however, become visible at higher laser wavelength.

Additional modes are calculated outside this spectral range. Below the main peak at 75 cm^{-1}, DFT predicts a low-frequency *E* mode at 17 cm^{-1} that cannot be verified experimentally due to the spectral limits of the employed setups. This mode corresponds to a rigid translation of the Au layer in the *xy* plane and is depicted in Fig. 7(a). A similar mode, albeit with a larger substrate contribution, is predicted by our calculations at 55 cm^{-1}, and it is found in the experiment at 66 cm^{-1}. A further mode corresponding to a vertical rigid translation of the Au layer is found at 33 cm^{-1}, which can be assigned to an experimental feature at 25 cm^{-1}. A phonon mode due to the rotation of the Au trimers [see Fig. 7(b)] is found at 54 cm^{-1} in the Raman measurement and 45 cm^{-1} in the calculations. While for all investigated modes the calculated Raman-scattering efficiency roughly matches the measured relative intensity, this mode appears in the spectra, although the calculations describe it as a Raman mode with vanishing scattering efficiency. We also observe that due to the typical tendency of the LDA to overestimate cohesive energies, phonon frequencies, and elastic moduli (overbinding) [70], this mode is strongly blueshifted in the LDA with respect to the GGA and experiment.

Above the high-intensity peak of *E* symmetry at 183 cm^{-1}, further peaks are found. Raman-active *E* modes at 205 and 221 cm^{-1} are predicted by the calculations and measured at 219 and 222 cm^{-1}. Experimentally measured high-frequency modes of 401 and 419 cm^{-1} are calculated as modes of *A* symmetry at 400 and 417 cm^{-1} that only involve Si atoms [see Fig. 7(d)]. The spectral range between these two groups is experimentally inaccessible due to the presence of the spectral intensity corresponding to the 2TA bulk phonons, and it will not be discussed in detail. All phonon modes localized on the Au layer affect the system's polarizability and are Raman-active. They are characterized by a frequency of at most 127 cm^{-1}. Modes with higher frequency are related to atomic displacements within the Si layer or both the Si and Au layers.

The good agreement between experiment and theory represents on the one hand a very strong argument for the CHCT structural model. On the other hand, it means that the spectral features measured in the frequency range between 20 and 200 cm^{-1} are true Au-induced phonon modes and they do not originate from second-order processes or other quasiparticles. Discrepancies in the relative intensity of measured and calculated Raman peaks might be traced to the approximations in our calculations and to spurious polarization components in the experiment due to a nonperfect scattering geometry.

The calculated spectrum for the (xy) polarization is not shown in this work, as it only features a subset of the Raman peaks appearing in Fig. 6. Indeed, while modes of *E* and *A* symmetry appear in the spectra obtained for (xx) polarization, only phonons of *E* symmetry appear in the (xy) polarization, according to the Raman selection rules. Modes not appearing in the (xy) polarization are exactly the modes that we have identified above as *A* modes due to the eigenvector symmetry and their missing degeneracy, which confirms the validity of our approach.

The good agreement between measured data and calculations according to the CHCT model allows for an assignment of the phonon modes of the Au-($\sqrt{3} \times \sqrt{3}$)$R30°$/Si(111) surface reconstruction. The assignment, based on the mode frequency, surface localization, symmetry, and Raman-scattering efficiency, is shown in Table II. The experimental peak positions for room temperature and low temperature together with the theoretical positions, intensities, symmetries, and localizations calculated within the DFT-GGA are listed. The mean deviation from the experimental values, amounting to 7.5 cm^{-1}, demonstrates a good agreement between theory and experiment and corroborates our mode assignment.

While the identification of the measured Raman peaks with the calculated phonons is unambiguous and clear for most modes, the mode at 54 cm^{-1} shows different symmetries in experiment and calculations and a vanishing scattering efficiency in our models, such as also the mode at 142 cm^{-1}. The reasons for this discrepancy might be manifold. Scanning

tunneling microscope (STM) measurements found domain walls for Au-($\sqrt{3} \times \sqrt{3}$)$R30°$/Si(111) [27]. It is likely that our prepared samples also have domain walls. Their density is unclear due to different preparation procedures, but it has most likely an effect on the vibrational modes. The theoretical calculations do not take domain walls into account. Deviations might arise because of this fact. We remark furthermore that our approach directly models surface localized vibrations of the Au-induced reconstruction of the Si(111) surface, while these are extrapolated in the experimental procedure as the difference of Au deposited and aged Si(111) surfaces. Furthermore, while our models represent spectra corresponding to an ideal backscattering configuration, in real experiments we deal with a slightly oblique angle of incidence of the laser light as well as a finite acceptance angle for the Raman light, so that unwanted light components might to some extent induce spurious features in the spectra.

IV. SUMMARY

Surface Raman spectroscopy together with theoretical models within DFT were employed to explore the vibrational properties of the Au-induced ($\sqrt{3} \times \sqrt{3}$)$R30°$ reconstruction of the Si(111) surface. Upon Au deposition, new Au-induced surface localized vibration eigenmodes appeared, in the spectral range from 20 to 450 cm^{-1}, comprising two dominant peaks of E symmetry at 75 and 183 cm^{-1}. Temperature-dependent measurements suggest that the system does not undergo a phase transition down to 20 K. First-principles calculations demonstrate the stability of the conjugate honeycomb-chained-trimer model (CHCT) among the structural patterns discussed in the literature. The calculation of the vibrational frequencies at the BZ center shows an eigenvalue spectrum that is compatible with the experimental results for the CHCT model, while larger deviations are predicted for the TT model. In addition to vibrational frequencies at the BZ center, the corresponding elongation patterns and the Raman intensities within different scattering geometries have been calculated for the CHCT and TT structure. Only the first model exhibits satisfactory agreement with the experimental results. All vibrational modes completely localized at the Au layer are found to be Raman-active and visible in the experiments. The good agreement between the measured phonon modes and the calculations corroborates the CHCT structural model and allows for an assignment of the measured spectral features to the calculated phonon modes.

ACKNOWLEDGMENTS

We gratefully acknowledge financial support from the Deutsche Forschungsgemeinschaft in the research units FOR 1162 (project Ge 1855/10-2) and FOR 1700 (projects Es 127/12-1 and Schm 1361/19). The Senatsverwaltung für Wirtschaft, Technologie und Forschung des Landes Berlin, the Ministerium für Innovation, Wissenschaft und Forschung des Landes Nordrhein-Westfalen, and the Bundesministerium für Bildung und Forschung are also acknowledged. Moreover, we thank R. Hölldobler for experimental support.

[1] P. C. Snijders and H. H. Weitering, Rev. Mod. Phys. **82**, 307 (2010).
[2] A. Tejeda, Y. Fagot-Révurat, R. Cortés, D. Malterre, E. G. Michel, and A. Mascaraque, Phys. Status Solidi A **209**, 614 (2012).
[3] C. Blumenstein, J. Schäfer, S. Mietke, and S. Meyer, Nat. Phys. **7**, 776 (2011).
[4] C. Blumenstein, J. Schäfer, M. Morresi, S. Mietke, R. Matzdorf, and R. Claessen, Phys. Rev. Lett. **107**, 165702 (2011).
[5] J. N. Crain, J. L. McChesney, F. Zheng, M. C. Gallagher, P. C. Snijders, M. Bissen, C. Gundelach, S. C. Erwin, and F. J. Himpsel, Phys. Rev. B **69**, 125401 (2004).
[6] S. C. Erwin and F. J. Himpsel, Nat. Commun. **1**, 1 (2010).
[7] S. Hasegawa, J. Phys.: Condens. Matter **22**, 084026 (2010).
[8] S. Cheon, T.-H. Kim, S.-H. Lee, and H. W. Yeom, Science **350**, 182 (2015).
[9] W. G. Schmidt, S. Wippermann, S. Sanna, M. Babilon, N. J. Vollmers, and U. Gerstmann, Phys. Status Solidi B **249**, 343 (2012).
[10] S. Sanna, C. Dues, W. G. Schmidt, F. Timmer, J. Wollschläger, M. Franz, S. Appelfeller, and M. Dähne, Phys. Rev. B **93**, 195407 (2016).
[11] C. Rogero, J. A. Martín-Gago, and J. I. Cerdá, Phys. Rev. B **74**, 121404 (2006).
[12] I. Engelhardt, C. Preinesberger, S. Becker, H. Eisele, and M. Dähne, Surf. Sci. **600**, 755 (2006).
[13] F. Timmer, R. Oelke, C. Dues, S. Sanna, W. G. Schmidt, M. Franz, S. Appelfeller, M. Dähne, and J. Wollschläger, Phys. Rev. B **94**, 205431 (2016).
[14] T. Frigge, B. Hafke, T. Witte, B. Krenzer, C. Streubühr, A. Samad Syed, V. Mikšić Trontl, I. Avigo, P. Zhou, M. Ligges, D. von der Linde, U. Bovensiepen, M. Horn-von Hoegen, S. Wippermann, A. Lücke, S. Sanna, U. Gerstmann, and W. G. Schmidt, Nature (London) **544**, 207 (2017).
[15] E. Jeckelmann, S. Sanna, W. G. Schmidt, E. Speiser, and N. Esser, Phys. Rev. B **93**, 241407 (2016).
[16] J. Kautz, M. W. Copel, M. S. Gordon, R. M. Tromp, and S. J. van der Molen, Phys. Rev. B **89**, 035416 (2014).
[17] D. Grozea, E. Bengu, and L. Marks, Surf. Sci. **461**, 23 (2000).
[18] F.-C. Chuang, C.-H. Hsu, H.-L. Chou, C. P. Crisostomo, Z.-Q. Huang, S.-Y. Wu, C.-C. Kuo, W.-C. V. Yeh, H. Lin, and A. Bansil, Phys. Rev. B **93**, 035429 (2016).
[19] M. Liebhaber, B. Halbig, U. Bass, J. Geurts, S. Neufeld, S. Sanna, W. G. Schmidt, E. Speiser, J. Räthel, S. Chandola, and N. Esser, Phys. Rev. B **94**, 235304 (2016).
[20] J. Y. Lee and H. M. Kang, J. Korean Phys. Soc. **55**, 2460 (2009).
[21] M. Chester and T. Gustafsson, Phys. Rev. B **42**, 9233 (1990).
[22] M. Chester and T. Gustafsson, Surf. Sci. **256**, 135 (1991).
[23] Y. Ding, C. Chan, and K. Ho, Surf. Sci. **275**, L691 (1992).
[24] H. M. Zhang, T. Balasubramanian, and R. I. G. Uhrberg, Phys. Rev. B **66**, 165402 (2002).
[25] T. Kadohira, J. Nakamura, and S. Watanabe, e-J. Surf. Sci. Technol. Nanotechnol. **2**, 146 (2004).
[26] D. Grozea, E. Landree, L. Marks, R. Feidenhans'l, M. Nielsen, and R. Johnson, Surf. Sci. **418**, 32 (1998).
[27] C. H. Patterson, J. Phys.: Condens. Matter **27**, 475001 (2015).

[28] H. Ibach and D. L. Mills, *Electron Energy Loss Spectroscopy and Surface Vibrations* (Academic, New York, 1982).
[29] H. Nienhaus and W. Mönch, Surf. Sci. **328**, L561 (1995).
[30] H. Nienhaus, Phys. Rev. B **56**, 13194 (1997).
[31] G. Benedek and J. Toennies, Surf. Sci. **299**, 587 (1994).
[32] M. Buongiorno Nardelli, D. Cvetko, V. De Renzi, L. Floreano, A. Morgante, M. Peloi, and F. Tommasini, Phys. Rev. B **52**, 16720 (1995).
[33] W. Daum, H. Ibach, and J. E. Müller, Phys. Rev. Lett. **59**, 1593 (1987).
[34] G. Lange, J. P. Toennies, P. Ruggerone, and G. Benedek, Europhys. Lett. **41**, 647 (1998).
[35] Y. Caudano, P. Thiry, and Y. Chabal, Surf. Sci. **502**, 91 (2002).
[36] L. J. Webb, S. Rivillon, D. J. Michalak, Y. J. Chabal, and N. S. Lewis, J. Phys. Chem. B **110**, 7349 (2006).
[37] B. Halbig, U. Bass, J. Geurts, M. Zinner, and K. Fauth, Phys. Rev. B **95**, 165115 (2017).
[38] N. Esser, K. Hinrichs, J. Power, and W. Richter, Surf. Sci. **427-428**, 44 (1999).
[39] N. Esser, Appl. Phys. A **69**, 507 (1999).
[40] K. Fleischer, S. Chandola, N. Esser, W. Richter, and J. F. McGilp, Phys. Rev. B **76**, 205406 (2007).
[41] E. Speiser, S. Chandola, K. Hinrichs, M. Gensch, C. Cobet, S. Wippermann, W. Schmidt, F. Bechstedt, W. Richter, K. Fleischer, J. F. McGilp, and N. Esser, Phys. Status Solidi B **247**, 2033 (2010).
[42] E. Speiser, N. Esser, S. Wippermann, and W. G. Schmidt, Phys. Rev. B **94**, 075417 (2016).
[43] M. Liebhaber, U. Bass, P. Bayersdorfer, J. Geurts, E. Speiser, J. Räthel, A. Baumann, S. Chandola, and N. Esser, Phys. Rev. B **89**, 045313 (2014).
[44] K. Hinrichs, A. Schierhorn, P. Haier, N. Esser, W. Richter, and J. Sahm, Phys. Rev. Lett. **79**, 1094 (1997).
[45] V. Wagner, J. Wagner, S. Gundel, L. Hansen, and J. Geurts, Phys. Rev. Lett. **89**, 166103 (2002).
[46] J. Räthel, E. Speiser, N. Esser, U. Bass, S. Meyer, J. Schäfer, and J. Geurts, Phys. Rev. B **86**, 035312 (2012).
[47] S. Sanna, S. Neufeld, M. Rüsing, G. Berth, A. Zrenner, and W. G. Schmidt, Phys. Rev. B **91**, 224302 (2015).
[48] T. Nagao, S. Hasegawa, K. Tsuchie, S. Ino, C. Voges, G. Klos, H. Pfnür, and M. Henzler, Phys. Rev. B **57**, 10100 (1998).
[49] T. C. Damen, S. P. S. Porto, and B. Tell, Phys. Rev. **142**, 570 (1966).
[50] *Light Scattering in Solids II: Basic Concepts and Instrumentation*, edited by M. Cardona and G. Güntherodt (Springer, Berlin, 1982), Vol. 50.
[51] D. Dornisch, W. Moritz, H. Schulz, R. Feidenhans'l, M. Nielsen, F. Grey, and R. L. Johnson, Phys. Rev. B **44**, 11221 (1991).
[52] G. F. Koster, J. O. Dimmock, R. G. Wheeler, and H. Statz, *Properties of the Thirty-two Point Groups* (MIT Press, Cambridge, MA, 1963).
[53] R. Loudon, Adv. Phys. **13**, 423 (1964).
[54] G. Kresse and J. Furthmüller, Comput. Mater. Sci. **6**, 15 (1996).
[55] G. Kresse and J. Furthmüller, Phys. Rev. B **54**, 11169 (1996).
[56] W. Kohn and L. J. Sham, Phys. Rev. **140**, A1133 (1965).
[57] D. M. Ceperley and B. J. Alder, Phys. Rev. Lett. **45**, 566 (1980).
[58] J. P. Perdew, J. A. Chevary, S. H. Vosko, K. A. Jackson, M. R. Pederson, D. J. Singh, and C. Fiolhais, Phys. Rev. B **46**, 6671 (1992).
[59] J. P. Perdew, K. Burke, and M. Ernzerhof, Phys. Rev. Lett. **77**, 3865 (1996).
[60] P. E. Blöchl, Phys. Rev. B **50**, 17953 (1994).
[61] G. Kresse and D. Joubert, Phys. Rev. B **59**, 1758 (1999).
[62] H. J. Monkhorst and J. D. Pack, Phys. Rev. B **13**, 5188 (1976).
[63] G. P. Srivastava, *The Physics of Phonons* (Adam Hilger, Bristol, 1990).
[64] M. Veithen, X. Gonze, and P. Ghosez, Phys. Rev. B **71**, 125107 (2005).
[65] M. Gajdoš, K. Hummer, G. Kresse, J. Furthmüller, and F. Bechstedt, Phys. Rev. B **73**, 045112 (2006).
[66] P. A. Temple and C. E. Hathaway, Phys. Rev. B **7**, 3685 (1973).
[67] K. Uchinokura, T. Sekine, and E. Matsuura, J. Phys. Chem. Solids **35**, 171 (1974).
[68] W. G. Schmidt, S. Glutsch, P. H. Hahn, and F. Bechstedt, Phys. Rev. B **67**, 085307 (2003).
[69] C. Hogan, E. Ferraro, N. McAlinden, and J. F. McGilp, Phys. Rev. Lett. **111**, 087401 (2013).
[70] A. van de Walle and G. Ceder, Phys. Rev. B **59**, 14992 (1999).